JGR Solid Earth

RESEARCH ARTICLE
10.1029/2019JB018789

Carbon Partitioning Between the Earth's Inner and Outer Core

Yunguo Li[1], Lidunka Vočadlo[1], Dario Alfè[1,2], and John Brodholt[1,3]

[1]Department of Earth Sciences, UCL, London, UK, [2]Dipartimento di Fisica Ettore Pancini, Università di Napoli Federico II, Monte S. Angelo, Napoli, Italy, [3]Centre for Earth Evolution and Dynamics, University of Oslo, Oslo, Norway

Key Points:
- The chemical potential of C in solid and liquid Fe was calculated using ab initio methods
- C almost completely partitions into liquid iron in the Fe-C binary system at Earth's core conditions
- The presence of C in the outer core may account for most of the density jump at the ICB

Correspondence to:
Y. Li,
yunguo.li@ucl.ac.uk

Citation:
Li, Y., Vočadlo, L., Alfè, D., & Brodholt, J. (2019). Carbon partitioning between the Earth's inner and outer core. *Journal of Geophysical Research: Solid Earth*, *124*, 12,812–12,824. https://doi.org/10.1029/2019JB018789

Received 26 SEP 2019
Accepted 13 DEC 2019
Accepted article online 14 DEC 2019
Published online 28 DEC 2019

Abstract Knowledge of the abundance and distribution of light elements in the core is fundamental to the understanding of the Earth and other planetary systems. Recent studies (Li et al., 2018; Mashino et al., 2019) suggest the particular importance of carbon for explaining core properties, yet knowledge of carbon partitioning between the outer and inner core is unknown. By using the quasiharmonic approximation, ab initio molecular dynamics, and thermodynamic integration techniques, we have computed the chemical potential of carbon in liquid Fe and solid *hcp*-Fe at core conditions. We find that substitutional carbon is more stable than interstitial carbon and other carbon defect cluster structures in solid Fe. Lattice strain and overcoordination effects lead to a high chemical potential of C in solid Fe compared to the liquid, and consequently carbon partitions almost completely into the liquid. We find that carbon can account for most of the density jump at the inner-core boundary. This provides an alternative mechanism to the necessity of an oxygen-rich outer core and may have significant implications for the composition and structure of the deep Earth.

1. Introduction

It is generally accepted that the Earth's core is made predominantly of Fe (Birch, 1952). However, the density of solid Fe at inner-core conditions is higher than the observed inner-core density by ~3 to 5% (Dubrovinsky et al., 2000), and that of liquid Fe under outer-core conditions is higher by ~5 to 10% (Anderson & Isaak, 2002; Stevenson, 1981). This requires that both the inner and outer core contain some light elements, with the concentration of light element being lower in the inner core. In addition to the density deficit, the observed seismic velocities of the core also differ from those determined for pure Fe from both theory and experiment (Mao et al., 2012; Martorell et al., 2013).

There are a number of approaches to identifying which light elements are in the core, including cosmochemical arguments (e.g., McDonough & Sun, 1995), matching the densities and velocities of the core to experimental and theoretical measurements of various Fe-alloys (e.g., Badro et al., 2014; Li et al., 2018), and matching the density jump between the inner and outer core. Another constraint is that the concentration of light element in the inner core is less than that of the outer core. In other words, the outer core must contain at least one element, which does not partition equally into the inner core. Dario Alfè et al. (2000) exploited this to suggest that oxygen must be a significant component of the outer core. This is because chemical potentials calculated from ab initio simulations show that both S and Si partition equally between solid and liquid Fe, whereas O partitions very strongly only into the outer core. Therefore, of the three elements studied, only oxygen satisfies the constraint of a lower light element concentration in the inner core than the outer core. This has led to the common assumption that the core must have at least a couple of wt% O.

However, there is increasing evidence that also C would not partition equally between the inner and outer core. By measuring the melting curves of Fe-Fe_3C-Fe_7C_3 up to 70 GPa, Lord et al. (2009) found that the eutectic point of iron and iron carbide and the C solubility in solid Fe are reduced considerably for pressures approaching ~50 GPa. The negligible amount of C in solid Fe in equilibrium with the Fe-C liquid means that C does not partition into solid Fe above ~50 GPa. On the other hand, Fei and Brosh (2014) performed experiments on the Fe-C system up to 20 GPa and fitted their data to a thermodynamic model. They found that while the eutectic composition does indeed decrease from 4.3 wt.% at ambient pressure to 3.5 wt.% at 20 GPa, an extrapolation of their results gave a eutectic point of 2.24 wt.% and a solubility of ~1.5 wt.% at 330 GPa. Their results suggest that a significant amount of C can be partitioned into *hcp*-Fe. Most recently,

Mashino et al. (2019) extended the pressure to 255 GPa and found a eutectic composition of 3 wt.% and a maximum solubility of 1 wt.% in *hcp*-Fe at ICB conditions. Their results suggest that C partitions more into liquid Fe, but their results generally agree with those of Fei and Brosh (2014). An attempt to estimate the partitioning theoretically was made by Zhang and Yin (2012), who used a two-phase method combined with ab initio molecular dynamics (AIMD) to obtain a partition coefficient of C between liquid Fe and silicate melt of 9±3 at 3200 K and 40 GPa. Other circumstantial evidence for the incompatibility of C in the inner core can be gleaned from Brodholt and Badro (2017). In Fe-melts they show that both S and Si substitute for Fe with no change in volume, whereas O and C strongly decrease the volume. Assuming that the same size mismatch happens in the solid phase, a consideration of lattice strain would suggest that the O and C should partition almost entirely into the outer core. Using the previously calculated atom volume of C (4.6 $Å^3$) in Fe at 360 GPa and 6500 K and a predictive model based on lattice strain (Blundy & Wood, 1994), we can obtain a strain energy of 3.2 eV by moving C from the liquid to the solid. This is even larger than that of O (Alfè, Gillan, & Price, 2002), and in metallic system this means C will be partitioned into the liquid.

So the evidence is pointing toward a nonunity partitioning of C between the inner and outer core although the amount of partitioning is still uncertain. In addition, none of the experiments were conducted at IC conditions, and as we show here, P&T has a very strong effect on the partition coefficient. Moreover, the magnitude of the partition coefficient is important since it controls the amount of C in the inner core and, therefore, how much of another light element is needed to explain inner-core velocities and densities.

In this study, we employed the quasiharmonic approximation (QHA), AIMD, and thermodynamic integration (TI) techniques to calculate the free energies of Fe-C alloys. The chemical potential of C in solid and liquid Fe and the partitioning were then derived under core conditions. We find that the substitutional *hcp*-Fe-C binary alloy is thermodynamically most stable at 360 GPa and 6500 K compared to other solid alloy structures. However, substitutional C has a much higher chemical potential in the solid than in liquid Fe. As a result, in this binary system, C almost completely partitions into the liquid Fe. We conclude, therefore, that C cannot be the sole light element in the core. Moreover, the lack of partitioning of C means that it can play a similar role suggested for O and explain the lower concentration of light element in the inner core. In other words, the outer core must contain some O and/or C, as well as other light element.

2. Methods

2.1. Speciation of Carbon in *hcp*-Fe

Impurity atoms in a solid can be substitutional or interstitial. They can also interact with other defects and develop defect clusters, which can dramatically change the physical and mechanical properties of the solid (Li, Korzhavyi, et al., 2017). At low pressure, the small size of the C atom means it is incorporated in an interstitial site, but density functional theory calculations show a switch to a preferred substitutional site at ~280 GPa (L. Huang et al., 2005). However, these calculations are only at 0 K and so it is not clear which mechanism is favored in the core, nor is it known whether another mechanism, such as defect clusters, would be more stable. Therefore, in this work, we explored substitutional C, the octahedral interstitial C, and their clusters in *hcp*-Fe at 360 GPa and high temperature.

Figure 1 shows the interstitial sites in *hcp*-Fe. We shall systematically ignore the tetrahedral interstitial site since this has already been shown to be ~5.5 eV less favorable than the octahedral interstitial site (Caracas, 2017). We denote the octahedral interstitial and substitutional C by C^i and C^s, respectively. We employed a $4\times4\times3$ *hcp* supercell containing 96 Fe atoms and created the substitutional alloy structures $Fe_{95}C^s_1$ and $Fe_{94}C^s_2$ and the interstitial alloy structures $Fe_{96}C^i_1$ and $Fe_{96}C^i_2$. The two C atoms were placed at the neighbouring lattice sites in $Fe_{95}C^s_2$ and at the neighbouring octahedral sites in $Fe_{96}C^i_2$. We also placed one C atom at the neighbouring octahedral site around a substitutional C atom to create a structure $Fe_{95}C^s_1C^i_1$, and we then placed more C atoms at the neighbouring octahedral sites to create structures including $Fe_{95}C^s_1C^i_2$, $Fe_{95}C^s_1C^i_3$, $Fe_{95}C^s_1C^i_4$, and $Fe_{95}C^s_1C^i_5$. There are six neighbouring octahedral sites around each lattice site in *hcp*-Fe. Therefore, there are one, three, three, three, and one symmetrically distinct structures for $Fe_{95}C^s_1C^i_1$, $Fe_{95}C^s_1C^i_2$, $Fe_{95}C^s_1C^i_3$, $Fe_{95}C^s_1C^i_4$, and $Fe_{95}C^s_1C^i_5$, respectively. In our calculations the lattice and ion positions were fully relaxed at 360 GPa and 0 K. After relaxation, C atoms in $Fe_{95}C^s_1C^i_1$, $Fe_{95}C^s_1C^i_2$, $Fe_{95}C^s_1C^i_3$, $Fe_{95}C^s_1C^i_4$,

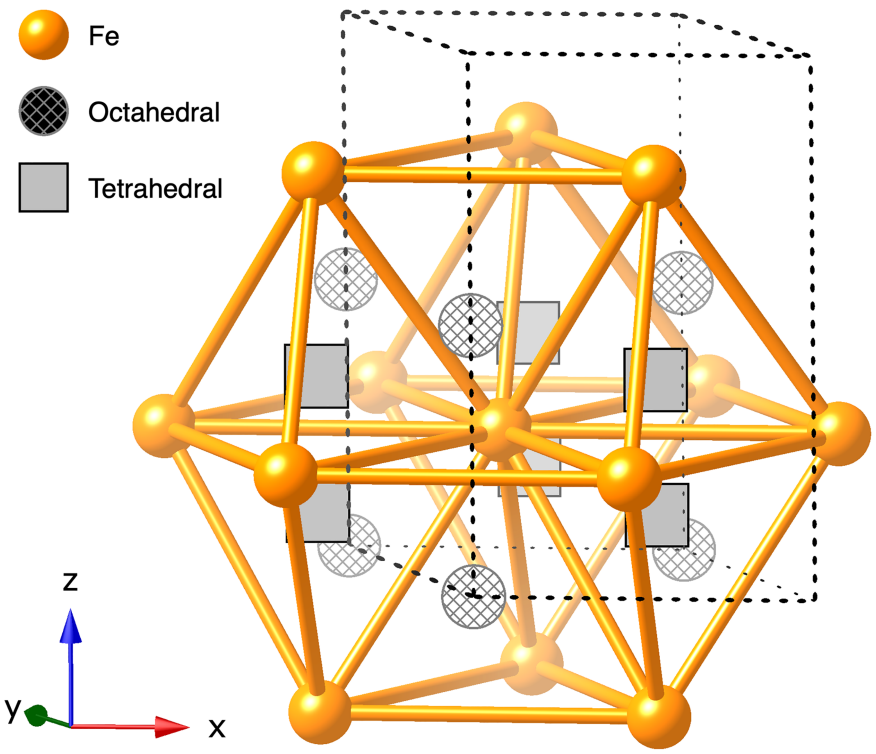

Figure 1. Illustration of interstitial sites in *hcp*-Fe.

and $Fe_{95}C_1^sC_5^i$ formed the *dimer*, *trimer*, *tetramer*, *pentamer*, and *hexamer* clusters, respectively, as can be seen in Figure 2.

2.2. Chemical Potential From the Quasiharmonic Approximation

We derived the Gibbs free energy of solid Fe-C alloys using the QHA method. The chemical potentials of different C speciations were then calculated from the quasiharmonic free energies.

For a system at a volume V and temperature T, the Helmholtz free energy can be written as

$$F(V,T) = U(V) + F_{ph}(V,T) + F_{el}(V,T) \tag{1}$$

where $U(V)$ is the internal energy—equivalent to the 0 K static total energy in the framework of ab initio calculations, $F_{ph}(V,T)$ is the vibrational free energy, and $F_{el}(V,T)$ is the electronic free energy. $F_{ph}(V,T)$ can be calculated by

$$F_{ph}(V,T) = k_B T \frac{1}{N_{\boldsymbol{q}}} \sum_{\boldsymbol{q}}^{N_{\boldsymbol{q}}} \frac{1}{N} \sum_{i}^{3N} \ln\left\{2\sinh\left[\frac{\hbar\omega_i(\boldsymbol{q})}{2k_B T}\right]\right\} \tag{2}$$

where N is the number of atoms in the primitive unit cell, $\boldsymbol{q}$ is the wavevector, and $N_{\boldsymbol{q}}$ is the number of wavevectors. k_B and $\hbar$ are the Boltzmann constant and the reduced Plank constant, respectively. $F_{el}(V,T)$ is defined as

$$F_{el}(V,T) = U_{el}(V,T) - TS_{el}(V,T) \tag{3}$$

where $U_{el}(V,T)$ is the thermal electronic energy and S_{el} is the electronic configurational entropy.

Once we obtain $F(V,T)$ as a function of V and T, pressure can be derived via

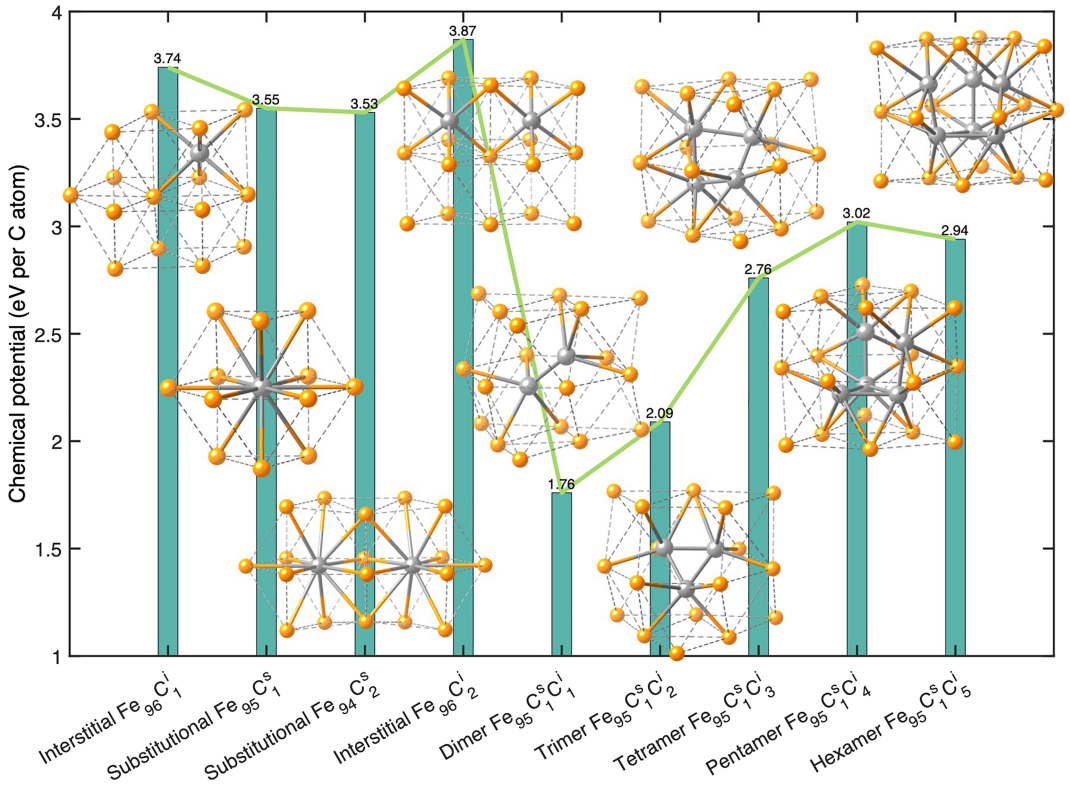

Figure 2. Chemical potential (referenced to the isolated single C atom) of different C speciations in *hcp*-Fe at 360 GPa and 0 K. The insert figures show the configurations of C speciations. The gold and gray colored balls indicate the Fe and C atoms, respectively.

$$p = -\left(\frac{\partial F(V,T)}{\partial V}\right)_T \tag{4}$$

The quasiharmonic Gibbs free energy is therefore $G(V,T) = F(V,T) - TS_{\text{conf}} + pV$ (S_{conf} is the configurational entropy in the alloy structures), which can be transformed to $G(p,T)$ as a function of p and T. The chemical potential of C in *hcp*-Fe was then calculated by

$$\mu_X(p,T) = \frac{G(p,T,N_A,N_X) - G(p,T,N_A)}{N_X} \tag{5}$$

where X and A denote the solute C and solvent Fe, respectively. N_A and N_X are the number of solvent and solute atoms.

2.3. Chemical Potential From Alchemical Free Energy Calculations

To account for the anharmonic effect, we employed the alchemical free energy approach. We used alchemical TI to calculate the carbon chemical potential in both the liquid Fe-C alloys and the substitutional Fe-C alloys. Unfortunately, this method cannot be applied to the interstitial and cluster structures.

The chemical potential of solute X in solvent A at specific T and p, ($\mu_X(p,T,c_X)$), can be written as

$$\mu_X(p,T,c_X) = \overline{\mu}_X(p,T,c_X) + k_B T \ln c_X \tag{6}$$

the first term on the right-hand side (RHS) is the pure component, and the second is from mixing entropy. Due to solute interactions, $\overline{\mu}_X(p,T,c_X)$ is concentration dependent and can be approximated by

$$\overline{\mu}_X(p,T,c_X) = \mu_X^{\dagger} + \alpha c_X + \beta {c_X}^2 \tag{7}$$

where $\mu_X^{\dagger}$ is concentration independent and α and β are coefficients. We will see below that the second-order

polynomial expansion of the pure component can well describe the concentration dependence. For the solid in this paper, we have ignored the interaction between solute atoms by using ordered alloy structures. This is still valid for the solid Fe-C system as the pair interaction energy is only 0.04 eV (calculated from energies of $Fe_{95}C_1^s$ and $Fe_{94}C_2^s$ as shown in Figure 2).

We calculated the chemical potential of C in both solid and liquid Fe using the alchemical free energy method described before (Alfè, Gillan, & Price, 2002; Li, Vočadlo, et al., 2017). Namely, the Gibbs free energy change $\mu_{XA}(p,T,c_X)$ of transmuting solvent A atoms (Fe in our case) into solute X atoms (C in our case) was calculated at the melting temperature of the pure solvent (T_m^0), and in this way we reference the solute chemical potential to the solvent chemical potential by

$$\mu_X(p,T,c_X) = \mu_{XA}(p,T,c_X) + \mu_A(p,T,c_X) \tag{8}$$

From the Gibbs-Duhem equation $c_X d\mu_X + (1-c_X)d\mu_A = 0$, we have

$$d\mu_A = -\frac{c_X}{1-c_X}d\mu_X = \left[-\frac{k_BT}{1-c_X} - \frac{(\alpha+2\beta c_X)c_X}{1-c_X}\right]dc_X = \left[\alpha + 2\beta(1+c_X) - \frac{k_BT+\alpha+2\beta}{1-c_X}\right]dc_X \tag{9}$$

and then,

$$\mu_A(p,T,c_X) = \mu_A^0 + (k_BT+\alpha+2\beta)\ln(1-c_X) + \alpha c_X + 2\beta c_X + \beta {c_X}^2 \tag{10}$$

This can be well approximated by $\mu_A(p,T,c_X) = \mu_A^0 - k_BTc_X + \beta(p,T){c_X}^2$ with an error <3% at c_X<0.05. To account for the nonlinearity of $\mu_{XA}(p,T,c_X)$ at higher concentrations, this approximation cannot be made. $\mu_{XA}(p,T,c_X)$ is therefore,

$$\mu_{XA}(p,T,c_X) = \mu_X^\dagger - \mu_A^0 + k_BT\ln c_X - (k_BT+\alpha+2\beta)\ln(1-c_X) - 2\beta c_X \tag{11}$$

Practically, it is more convenient to calculate μ_{XA} at constant volume rather than at constant pressure. At constant volume $\bar{v}$, we have

$$\begin{aligned}\mu_{XA}(\bar{v},T,c_X) &= F(N_A-1,N_X+1) - F(N_A,N_X)\\ &= -k_BT\ln\left(\frac{N_A}{N_X}\right) + 3k_BT\ln\left(\frac{\Lambda_X}{\Lambda_A}\right) - k_BT\ln\left\{\frac{\int_V d\boldsymbol{R}\exp[-U(N_A-1,N_X+1;\boldsymbol{R})/(k_BT)]}{\int_V d\boldsymbol{R}\exp[-U(N_A,N_X;\boldsymbol{R})/(k_BT)]}\right\}\\ &= k_BT\ln(c_X) + k_BTc_X + 3k_BT\ln\left(\frac{\Lambda_X}{\Lambda_A}\right) + m(\bar{v},T,c_X)\end{aligned} \tag{12}$$

where the Helmholtz free energy $F(N_A,N_X)$ is for the system with N_A solvent atoms and N_X solute atoms, $F(N_A-1,N_X+1)$ is for the system with one less solvent atom and one more solute atom, and $U(N_A,N_X;R)$ and $U(N_A-1,N_X+1;R)$ are the total energy functions for the two systems, respectively (Alfè, Gillan, & Price, 2002). Λ_X and Λ_A are the thermal wavelengths $(h/(2\pi M k_BT)^{1/2}$, h is Planck constant, and M is the atomic mass) of X and A, respectively. $m(\bar{v},T,c_X)$ is the only quantity that needs to be treated by ab initio calculations, and

$$m(\bar{v},T,c_X) = -k_BT\ln\left\{\frac{\int_V d\boldsymbol{R}\exp[-U(N_A-1,N_X+1;\boldsymbol{R})/(k_BT)]}{\int_V d\boldsymbol{R}\exp[-U(N_A,N_X;\boldsymbol{R})/(k_BT)]}\right\} \tag{13}$$

Equating equations (11) and (12), we have

$$3k_BT\ln\left(\frac{\Lambda_X}{\Lambda_A}\right) + m(\bar{v},T,c_X) = \mu_X^\dagger - \mu_A^0 - k_BTc_X - (k_BT+\alpha+2\beta)\ln(1-c_X) - 2\beta c_X \tag{14}$$

$\mu_X^\dagger - \mu_A^0$, α and β can be obtained by fitting equation (14) with calculated $m(\bar{v},T,c_X)$. In practice, we deal with the number of atoms rather than the concentration c_X. We therefore, introduce another quantity $W(N,N_X)$ (Alfè, Gillan, & Price, 2002) as

$$W(N,N_X) = -k_B T \ln\left\{\frac{\int_V d\boldsymbol{R}\exp[-U(N-N_X,N_X;\boldsymbol{R})/(k_B T)]}{\int_V d\boldsymbol{R}\exp[-U(N,0;\boldsymbol{R})/(k_B T)]}\right\} \quad (15)$$

which can be calculated by the TI technique

$$W(N,N_X) = \int_0^1 d\lambda \langle U_1 - U_0\rangle_\lambda \quad (16)$$

where the total energy functions $U_1(\mathrm{R}) = U(N-N_X,N_X;\mathrm{R})$ and $U_0(\mathrm{R}) = U(N,0;\mathrm{R})$. $W(N,N_X)/N_X$ equals to $m(\bar{v},T,c_X)$ at N_X approaching 0. We can obtain $m(\bar{v},T,c_X)$ from the calculated concentration dependent $W(N,N_X)$ by

$$\frac{\partial m(\bar{v},T,c_X)}{\partial c_X} = 2\frac{\partial\left[\frac{W(N,N_X)}{N_X}\right]}{\partial c_X} \quad (17)$$

This is because the calculated free energy difference at N_X/N corresponds to the chemical potential difference at $N_X/2N$, according to the definition of chemical potential.

Now we have to convert $\mu_{XA}(\bar{v},T,c_X)$ to $\mu_{XA}(p,T,c_X)$ (Alfè, Gillan, & Price, 2002). A relationship exists between $m(\bar{v},T,c_X)$ and $m(p,T,c_X)$ as

$$(\partial m(p,T,c_X)/\partial c_X)_P = (\partial m(\bar{v},T,c_X)/\partial c_X)_V - nB_T(v_X - v_A)^2 \quad (18)$$

where v_X and v_A are the volumes of solute and solvent atoms, respectively. $n = N/V$ is the atomic number density. v_X can be calculated via $v_X = dp \cdot V/B_T + v_A$. We can rewrite equations (14) as

$$3k_B T\ln\left(\frac{\Lambda_X}{\Lambda_A}\right) + m(\bar{v},T,c_X) - nB_T(v_X - v_A)^2 c_X = \mu_X^\dagger - \mu_A^0 - k_B T c_X - (k_B T + \alpha + 2\beta)\ln(1-c_X) - 2\beta c_X \quad (19)$$

α and β can be obtained by fitting the RHS to the calculated left-hand side.

2.4. Simulation Details

Density functional theory calculations were performed by using the Vienna Ab initio Simulation Package (VASP) with the implemented projector augmented wave method (Blöchl, 1994; Georg Kresse & Furthmüller, 1996; G. Kresse & Hafner, 1993; G. Kresse & Joubert, 1999). Fe-$3p^6 3d^7 4s^1$ and C-$2s^2 2p^2$ were treated as valence states, and the planewave cutoff energy was set to be 400 eV. The generalized gradient approximation with the Perdew-Wang scheme (Perdew & Wang, 1992) was used to treat the exchange-correlation interactions. Single-particle orbitals were populated according to the Fermi-Dirac statistics. Plane-wave basis cutoff energy was set as 400 eV.

For the defect cluster calculations with the $4 \times 4 \times 3$ *hcp* supercell, a $4 \times 4 \times 4$ Monkhorst-Pack mesh was used for structure relaxation and phonon calculations. The lattice and ion positions were fully relaxed at 360 GPa using the energy and force convergence criteria 1×10^{-8} eV and 1×10^{-4} eV/Å, respectively. The volume was then changed to create 10 structures, and both the lattice shape and ionic positions were fully relaxed. Phonon calculations were performed by using both the PHON code (Dario Alfè, 2009) and Phonopy code (Togo & Tanaka, 2015) with the direct force constant approach.

For the alchemical TI calculations, we employed a $4 \times 4 \times 2$ *hcp* supercell and used an energy convergence criteria 2×10^{-5} eV. We performed constant volume AIMD calculations (NVT) to calculate the free energy change $W(N,N_X)/N_X$ and hence μ_{XA} at ~360 GPa and 6500 K (corresponding to an atom volume V/N=6.999 Å^3 for liquid and 6.859 Å^3 for solid). The pure Fe supercells have been equilibrated under the NVT ensemble for over 10 ps. We calculated $W(N,N_X)/N_X$ by starting with the pure Fe system and transmuting 1, 2, 3, and 4 atoms for the solid and 1, 2, 3, and 8 atoms for the liquid. Five equally spaced λ (0.0, 0.25, 0.5, 0.75, and 1.0) were used for TI; the number of λ used is sufficient to converge the integration within the statistical error, since the integration along the path for the free energy change $W(N,N_X)/N_X$ is smooth.

At each λ, we calculated separately the energies and forces for the pure system and alloy system sharing the same configuration and trajectory, and the configuration was updated after every MD step according to the weighted forces from the two separate systems. The mass of C atoms was set equal to the mass of iron as explained in Pozzo et al. (2019). The Verlet algorithm (with a time step of 1.0 fs) was used to integrate classical Newton's equations of motion. The Nosé thermostat was used for temperature control (Di Tolla & Ronchetti, 1993; Nosé, 1984). Most MD runs are over 10 ps, and we dropped the first 2 ps except for the solid $Fe_{60}C_4$. The solid $Fe_{60}C_4$ supercell melted after ~2 ps equilibration at $\lambda = 1.0$ and has a large uncertainty for $\langle U_1 - U_0 \rangle_{1.0}$. We examined the root-mean-squared displacement to ensure the state does not change.

$\langle U_1 - U_0 \rangle_\lambda$ were initially calculated by sampling the Brillouin zone with the Γ-point and then corrected to the sampling with a $3 \times 3 \times 2$ Monkhorst-Pack mesh, via the TI scheme (D. Alfè et al., 2001)

$$\Delta F^{G\to K} = \int_0^1 d\lambda \left\langle U^k - U^G \right\rangle_G \approx \left\langle U^k - U^G \right\rangle_G - \frac{1}{2k_B T} \left\langle \delta U^2 \right\rangle_G \tag{18}$$

where $\Delta F^{G \to K}$ is the correction from the Γ-point to the multi-K-point (G → K) sampling. U^k and U^G are the free energies of the Γ-point and multi-K-point calculations, respectively. δU is

$$\delta U = \left\langle U^k - U^G - \left\langle U^k - U^G \right\rangle_G \right\rangle_G \tag{19}$$

We resampled 100 snapshots spaced by 50 time steps with a $3 \times 3 \times 2$ Monkhorst-Pack mesh.

A pressure correction as a result of the Γ to multi-K-point sampling was also applied for calculations of v_X and $nB_T(v_X - v_A)^2 c_X$. We used B_T=1375 GPa for solid Fe (Li et al., 2018) and 1318 GPa for liquid Fe (Vočadlo et al., 2003), respectively. For pure iron, the calculated pressure P (with G → K correction) deviates from the target pressure P^0 of 360 GPa. This also requires a recalibration of μ_A^0 with a correction of $(P - P^0)v_A$ to μ_{XA}.

3. Results

3.1. Stability of Different Carbon Speciations

The free energies of *hcp*-Fe-C alloys with different C speciations were plotted in Figure 3, and the chemical potentials of C at 0 K were plotted in Figure 2 together with the cluster configurations. As can be seen, the static calculations show that the substitutional structure is more stable than the interstitial structure, in agreement with previous studies (L. Huang et al., 2005). However, the dimer structure is actually the most stable one at 0 K. The chemical potential of C in the dimer structure is lowered by 1.79 eV than that in the substitutional structure. The other C clusters also have lower chemical potentials than the substitutional C. In addition, the two substitutional structures $Fe_{95}C_1^s$ and $Fe_{94}C_2^s$ have almost the same C chemical potential, suggesting little interaction between substitutional C atoms. The C chemical potential in $Fe_{96}C_2^i$ is higher than that in $Fe_{96}C_1^i$ by 0.14 eV, implying a repulsive interaction between interstitial C atoms.

As can be seen in Figure 3, the harmonic approximation (which assumes the vibrational frequencies are independent of volume) results at 6500 K show that the dimer is still more stable than both the substitutional and the interstitial. But, the difference between the dimer and the substitutional is much lower than that at 0 K. The loss of configurational entropy due to clustering and the strong bonding between C atoms tend to increase the Gibbs free energy of the dimer structure at high temperatures. Thus, temperature destabilizes the dimer structure. Under the QHA (which treats the volume-dependent vibrational frequencies explicitly) at 6500 K, the stability of the dimer structure is further weakened and the substitutional structure becomes slightly more stable than the dimer structure. This is because the electronic free energy also destabilizes the dimer structure. In other words, at core conditions, the substitutional mechanism is the most likely incorporation mechanism for C in hcp Fe.

3.2. Free Energy of the Liquid and Substitutional Fe-C Alloys

In Table 1, we summarize the calculated key quantities described above for the alchemical TI calculations. In Figure 4 we plot the calculated integrand $\langle U_1 - U_0 \rangle_\lambda$ for all our examined samples. The smoothness of the integrand suggests that there is no phase change during the reversible process. Numerical integration was

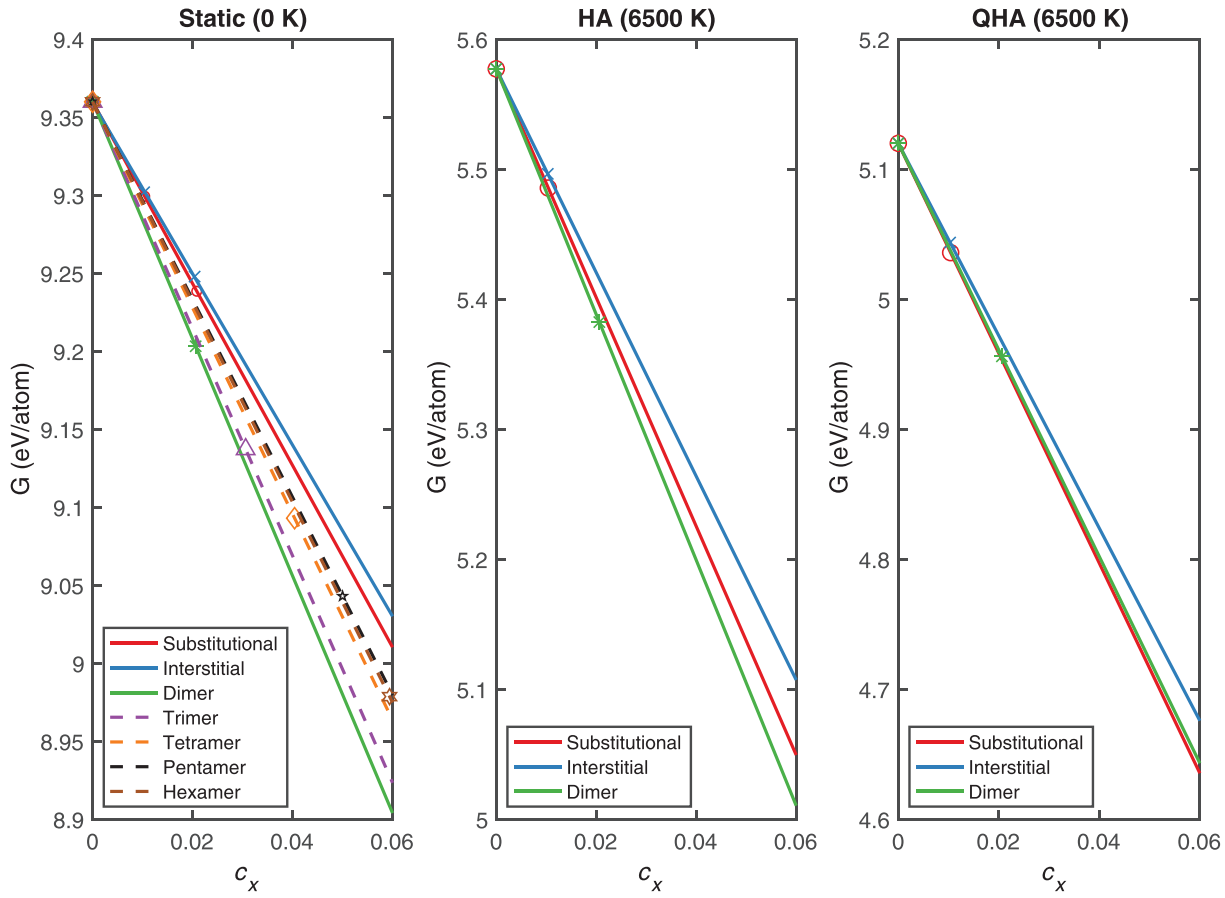

Figure 3. Gibbs free energy of Fe—C alloys with different carbon speciations from the static, harmonic approximation (HA) and quasiharmonic approximation (QHA) calculations at 360 GPa.

preceded based on a spline fitting. The difference with polynomial integration is less than 0.02 eV. The integration Figure 5 shows the calculated left-hand side in comparison with the fitted RHS of equation (19). The good match between the calculated and fitted data shows that the carbon chemical potential can be well described by the second-order polynomial.

We derived the chemical potential of C from its difference to that of pure Fe (μ_A^0) as described above. μ_A^0 is 4.921 and 4.931 eV for solid and liquid Fe at 360 GPa and 6500 K (Alfè, Price, & Gillan, 2002), respectively. The calculated Gibbs free energies and C chemical potentials for the substitutional solid and liquid Fe-C alloys are plotted in Figure 6. As can be seen, the chemical potential of C in solid Fe is much higher than

Table 1
The Calculated Carbon Atom Volume v_X and Its Uncertainty $\sigma(v_X)$, $W(N, N_X)/N_X$ and Its Uncertainty $\sigma(W(N, N_X)/N_X)$, Γ to Multi-K-Point Sampling Correction $\Delta F^{G \to K}$ to $W(N, N_X)/N_X$, Correction $(P - P^0)v_A$ Due to Pressure Deviation From 360 GPa for Pure Fe, Chemical Potential Parameters α, β, and $\mu_X^\dagger - \mu_A^0$, in Solid and Liquid Fe at ~360 GPa and 6500 K

State	Supercell	v_X (Å^3)	$\sigma(v_X)$ (Å^3)	$W(N, N_X)/N_X$ (eV)	$\sigma(W(N, N_X)/N_X)$ (eV)	$\Delta F^{G \to K}$ (eV)	$(P - P^0)v_A$ (eV)	$\mu_X^\dagger - \mu_A^0$ (eV)	α	β
Liquid	$Fe_{63}C_1$	3.597	0.212	−10.144	0.448	−0.038	−0.157	−8.568	−73.940	707.707
	$Fe_{62}C_2$	3.582	0.135	−10.387	0.349	−0.075	−0.167			
	$Fe_{61}C_3$	3.578	0.085	−10.547	0.215	−0.048	−0.108			
	$Fe_{56}C_8$	3.769	0.029	−10.028	0.138	−0.242	−0.140			
Solid	$Fe_{63}C_1$	4.391	0.172	−7.013	0.242	−0.698	−0.127	−4.958	−136.749	2036.666
	$Fe_{62}C_2$	4.432	0.084	−7.695	0.184	−1.176	−0.126			
	$Fe_{61}C_3$	4.453	0.064	−7.916	0.175	−1.506	−0.116			
	$Fe_{60}C_4$	4.556	0.089	−8.085	0.164	−2.167	−0.125			

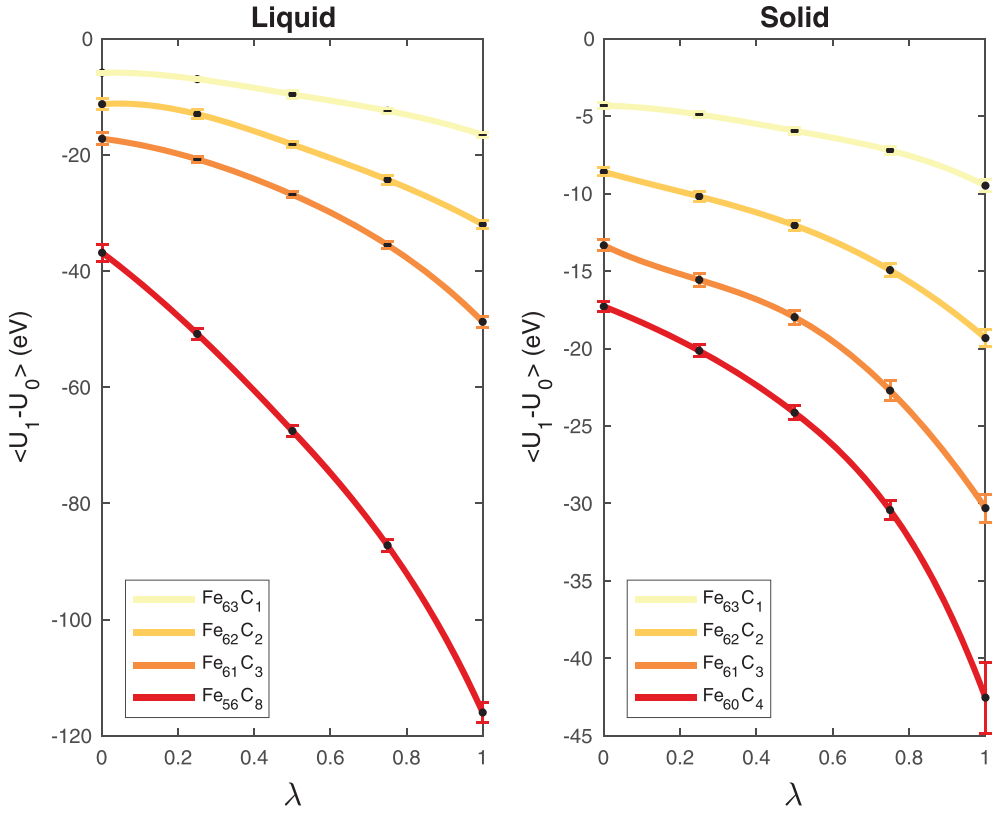

Figure 4. The calculated integrand $\langle U_1 - U_0 \rangle_\lambda$ as a function of λ used for calculations of the free energy difference $W(N, N_X)/N_X$ in liquid and solid iron. The curves are spline fittings.

that in liquid Fe at all concentrations. At the infinitesimal concentration limit, the difference is 3.61 eV. Although we did not explicitly treat the solute-solute interactions in solid Fe-C alloys, it is unlikely to make a significant difference given such a large gap between solid and liquid C chemical potentials.

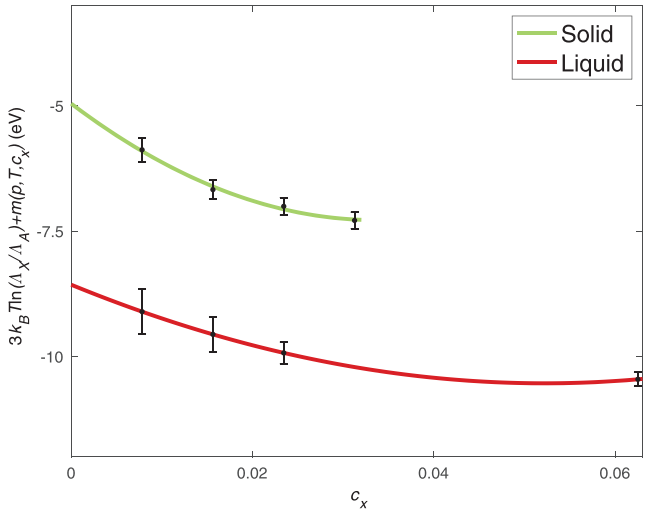

Figure 5. The calculated left-hand side of equation (14) $\left(3k_BTln\left(\frac{\Lambda_X}{\Lambda_A}\right) + m(p, T, c_X)\right)$ shown as dots with the error bar. The curves are fits (corresponding to the right-hand side of equation (14)). Fitting parameters are listed in Table 1.

4. Discussion

4.1. Carbon in Solid and Liquid Fe

We can perform the common tangent calculation on the Gibbs free energy curves of the substitutional solid and liquid Fe-C alloys in Figure 6 to determine the partition coefficient for C. We obtained a partition coefficient of 15,973 for carbon between liquid and solid Fe, implying a negligible concentration of C in *hcp*-Fe in equilibrium with liquid Fe at ~360 GPa. This is consistent with the large difference of C chemical potential between the substitutional solid and liquid Fe-C alloys. One thing to note is that we only performed the full anharmonic TI correction on the substitutional mechanism. However, the magnitude of this correction is only −0.20 eV compared to the QHA result. Since we would expect a similar anharmonic correction to other incorporation mechanisms of C in solid Fe, the chemical potential of C in solid Fe would always be much higher than that in the liquid Fe regardless of the specific mechanism. So allthough we did not perform full TI calculations on the dimer structure, it should not be able to prevent us from concluding that C mostly partitions strongly into liquid Fe rather than into the solid.

The average coordination number of 9.8 (see Figure 7) for C in solid Fe suggests that the substitutional C is not well confined at the lattice site.

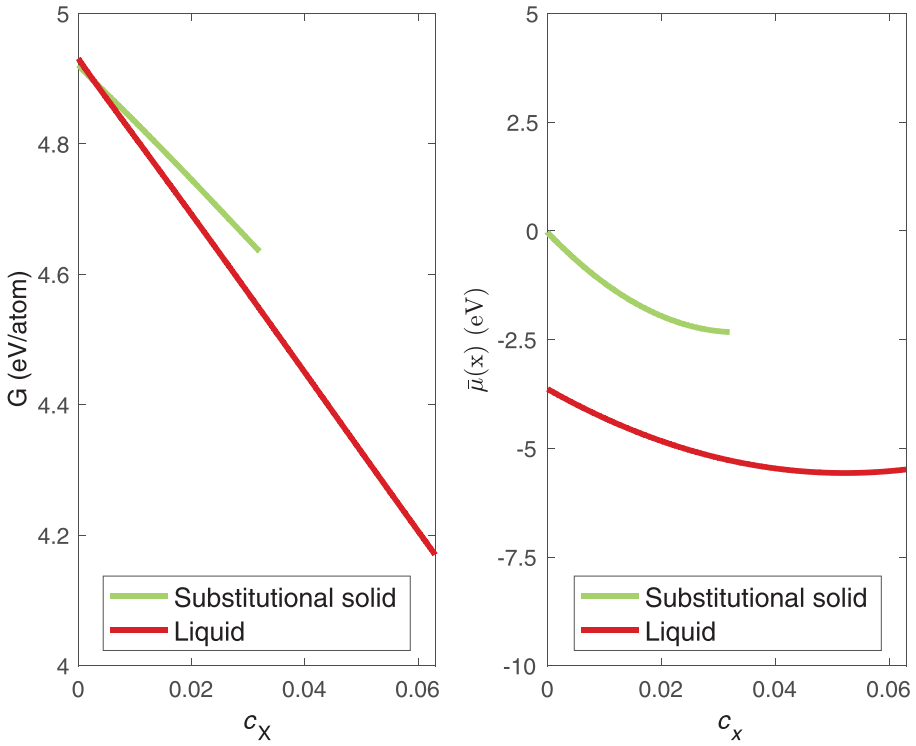

Figure 6. (a) Calculated Gibbs free energy of the substitutional solid and liquid Fe—C alloys as a function of molar fraction c_x of carbon. (b) The pure component ($\bar{\mu}_x$) of C chemical potential in the substitutional solid and liquid Fe—C alloys.

The C—Fe bond length of 1.90 Å is also less than that of Fe-Fe of 2.09 Å in solid (see the radial distribution function in Figure 7). Clearly, substitutional C creates a significant lattice distortion. Apart from the low coordination number of C in solid iron, the C-Fe bond is larger by 0.17 Å (Figure 7) than that in liquid Fe, indicating that the lattice vacancy is too large for C.

Fe atoms in the liquid remain in close-packed coordination with almost the same coordination number of 12 as in solid. C atoms in liquid Fe have an average coordination number of 6.8 as can be seen in Figure 7. This suggests that C atoms in liquid Fe are inside the octahedron of Fe. The Fe—C—Fe bond angle has two peaks at 71 and 129° as shown in Figure 7, implying the Fe octahedron is likely to be in a distorted shape. The deflection from the bond angle of 90° in the octahedron is probably because C with π electrons prefers tetrahedral coordination. The radial distribution function shows C—C has a peak at 1.39 Å, suggesting an attractive interaction between C atoms.

From the structural analyses above, it can be inferred that the C—Fe bond is subject to strain and C is overcoordinated with Fe in the solid. Therefore, the high C chemical potential in the substitutional Fe—C solid has contributions from both the strain effect and the chemical bonding. Notably, the behavior of C in Fe shares many similarities with O, which has an atomic volume of 4.25 $Å^3$ in liquid Fe and 4.62 $Å^3$ in solid Fe at 370 GPa and 7000 K (Alfè, Gillan, & Price, 2002). The volumes of both C and O are much lower than that of Fe, and significant lattice distortion can be expected as they enter *hcp*-Fe in the substitutional form. The molar volume of liquid Fe—O alloy is found to be insensitive to pressure and O has a coordination number of ~6 (Ichikawa & Tsuchiya, 2015; Posner et al., 2017), implying that O is also at the center of the Fe octahedron in liquid Fe. Partition calculations also suggest that O almost completely partitions into the liquid Fe rather than *hcp*-Fe (Alfè, Gillan, & Price, 2002).

The results above are strictly calculated at 360 GPa, but we can also apply our results to 330 GPa (the current ICB pressure). From 360 GPa to the ICB pressure 330 GPa, the substitutional C chemical potential in the solid Fe drops by 0.83 eV at 6500 K from the QHA result. Even if we make the unlikely assumption that the chemical potential of C in liquid Fe does not decrease from 360 to 330 GPa, the C chemical potential in solid Fe is still higher than that in the liquid Fe by 2.78 eV. However, at much lower pressures and

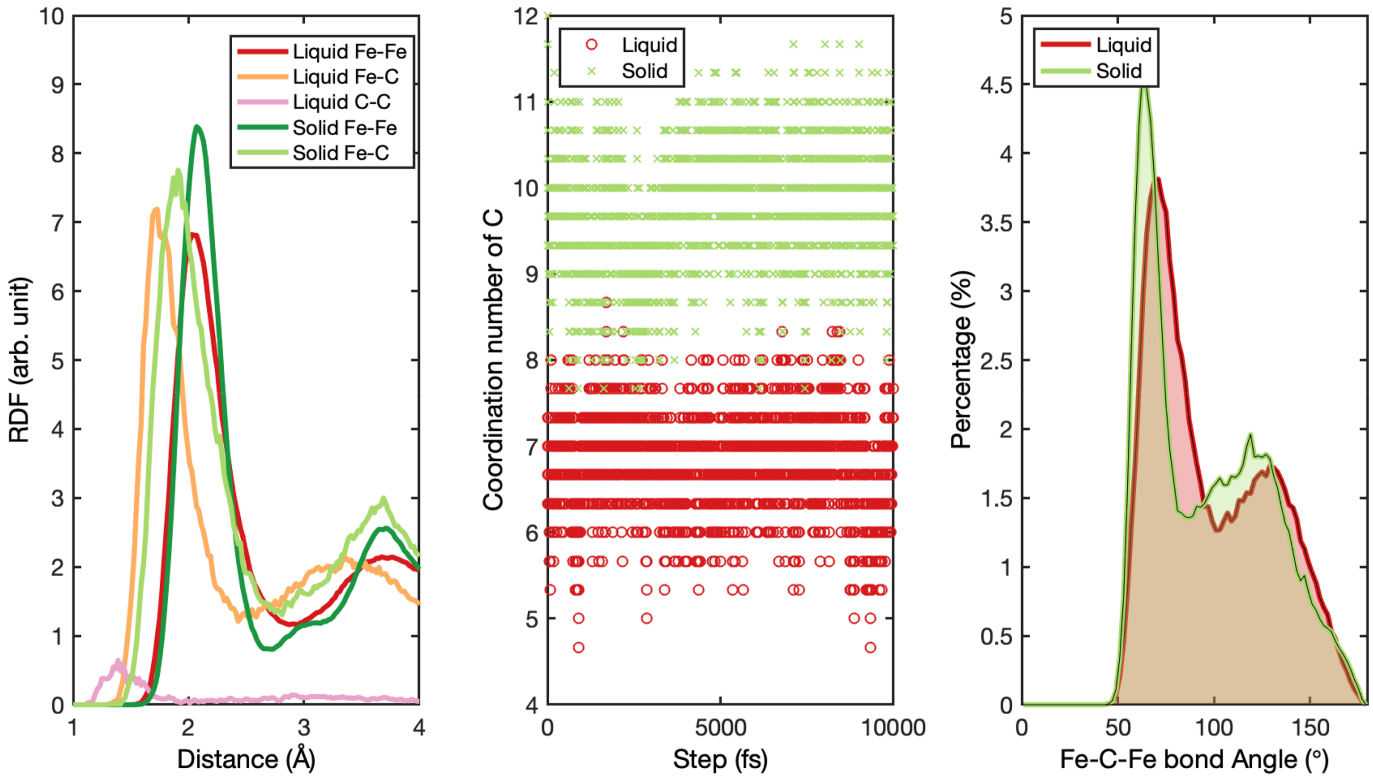

Figure 7. The radial distribution function (RDF), coordination number of C, and Fe—C—Fe dihedral angle in solid and liquid $Fe_{61}C_3$. The coordination number was searched with a cutoff distance up to the first valley position in RDF, and for C it was searched with a bond length of 1.73 ± 0.42 Å in solid and 1.90 ± 0.50 Å in liquid. The averaged coordination number for C is 9.8 in liquid Fe and 6.8 in solid Fe.

temperatures, the carbon cluster or interstitial configurations are expected to be more stable than the substitutional configuration, which may allow some C to be partitioned into the solid. This possibility needs to be investigated in further studies, but at core pressures C partitions almost entirely into the liquid.

Our results are somewhat different from the experimental results, which show that hcp Fe can take up to about 1 to 2 wt% C. However, all of these are at significantly lower pressure and temperature, and our results show that the chemical potential of C in Fe is a strong function of temperature and pressure.

4.2. Implications for the Core

So far, only multicomponent alloys with C have been found to match the observed inner-core seismic properties (Li et al., 2018). Yet here we show that C partitions almost entirely into the outer core. While these may appear to be contrary conclusions, it must be noted that this present study only looks at the binary system, while our earlier work found compositions matching the seismic observations for ternary and higher systems. It is possible that the partitioning of carbon within a ternary or quaternary alloy may be substantially different to that for the pure Fe—C binary system studied here. For instance, experimental results on carbon partitioning between magma ocean and core-forming alloy liquid show that the presence of sulfur may dramatically change the solubility limit of carbon in the liquid iron alloy as well as partitioning coefficient (Tsuno et al., 2018). However, what happens at inner core P&T is still unknown. While Fe_7C_3 may be ruled out as the solid phase (Li et al., 2016), other carbides may exist that match the seismic observations and have different partitioning behavior.

Nevertheless, taken at face value, our results suggest that C does not partition into the inner core. As such, C can be responsible for the density jump at the ICB, and the expulsion of C from the inner core may also play a part in the generation of the geodynamo. In Figure 8 we plot the density difference between solid and liquid Fe—C alloys in equilibrium and compare it with the ICB density jump. Assuming that carbon is the only light element in the core, about 6.5–8.8 at.% C is required to match the density jump at the ICB,

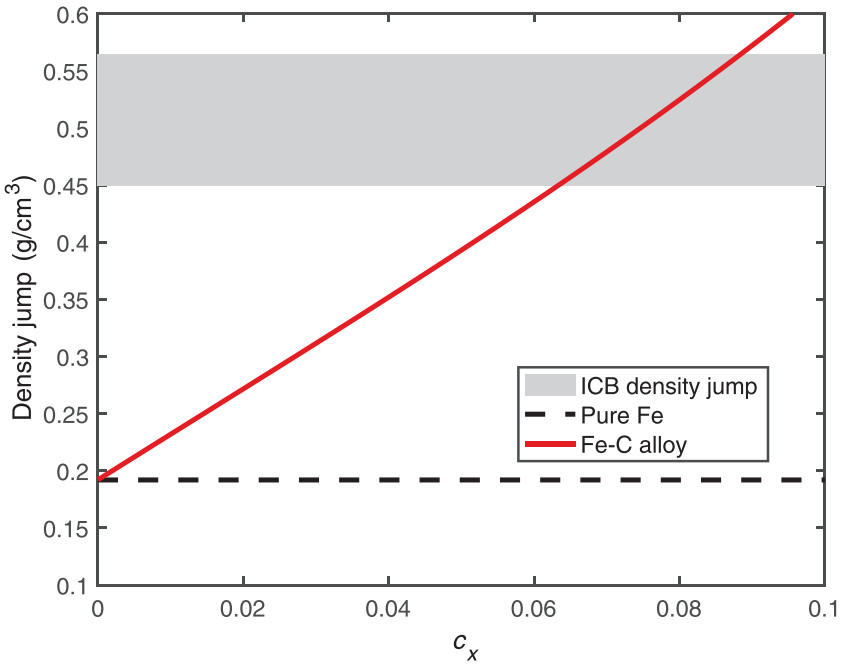

Figure 8. The calculated density difference between solid and liquid states for pure Fe and Fe—C alloys under core conditions, in comparison with the estimates for the density jump at inner-core boundary (shaded region; Koper & Pyle, 2004; Tkalčić et al., 2009).

equivalent to 1.5–2.0 wt.% C in the outer core. This is close to many estimations of carbon budget in the core (Wood et al., 2013). Although our work does not negate the need for a significant amount of O in the core (H. Huang et al., 2011), it shows that O is not necessary to explain the ICB density jump. Together with other light elements, the existence of C may also explain the density deficit of outer core.

5. Conclusions

We have studied *hcp*-Fe—C alloys with different incorporation mechanism including the substitutional, interstitial, and other carbon defect clusters under QHA. The substitutional structure is the most stable one at 360 GPa and 6500 K. We performed AIMD calculations and TI to obtain the chemical potential of C in both liquid and solid Fe. We found that the C chemical potential in solid is higher than that in liquid by 3.61 eV at the infinitesimal concentration limit. This is because C is subjected to extra strain and overcoordination in solid *hcp*-Fe. Consequently, C will almost completely partition into liquid Fe in the Fe—C binary system, which can account for most of the density jump at the ICB and reduce the necessity for significant amounts of O in the core.

Acknowledgments
This study was funded by NERC grant NE/M015181/1. Computation resources were provided by the ARCHER supercomputer facility. We thank anonymous reviewers for their valuable and constructive suggestions. Original data were shown in Table 1 and Figures 2 and 4, from which data on Figures 3, 5, and 6 can be derived. Raw simulation outputs can be accessed here https://doi.org/10.5522/04/10783589.

References

Alfè, D. (2009). PHON: A program to calculate phonons using the small displacement method. *Computer Physics Communications*, *180*(12), 2622–2633. https://doi.org/10.1016/j.cpc.2009.03.010

Alfè, D., Gillan, M. J., & Price, G. D. (2000). Constraints on the composition of the Earth's core from ab initio calculations. *Nature*, *405*(6783), 172–175.

Alfè, D., Gillan, M. J., & Price, G. D. (2002). *Ab initio* chemical potentials of solid and liquid solutions and the chemistry of the Earth's core. *Journal of Chemical Physics*, *116*(16), 7127–7136.

Alfè, D., Price, G. D., & Gillan, M. J. (2001). Thermodynamics of hexagonal-close-packed iron under Earth's core conditions. *Physical Review B*, *64*(4), 045123–045123.

Alfè, D., Price, G. D., & Gillan, M. J. (2002). Iron under Earth's core conditions: Liquid-state thermodynamics and high-pressure melting curve from ab initio calculations. *Physical Review B*, *65*(16), 165118–165118.

Anderson, O. L., & Isaak, D. G. (2002). Another look at the core density deficit of Earth's outer core. *Physics of the Earth and Planetary Interiors*, *131*(1), 19–27.

Badro, J., Côté, A. S., & Brodholt, J. P. (2014). A seismologically consistent compositional model of Earth's core. *Proceedings of the National Academy of Sciences*, *111*(21), 7542–7545.

Birch, F. (1952). Elasticity and constitution of the Earth's interior. *Journal of Geophysical Research*, *57*(2), 227–286.

Blöchl, P. E. (1994). Projector augmented-wave method. *Physical Review B*, *50*(24), 17,953–17,953.

Blundy, J., & Wood, B. (1994). Prediction of crystal–melt partition coefficients from elastic moduli. *Nature*, *372*(6505), 452–454.
Brodholt, J., & Badro, J. (2017). Composition of the low seismic velocity E′ layer at the top of Earth's core. *Geophysical Research Letters*, *44*, 8303–8310.
Caracas, R. (2017). The influence of carbon on the seismic properties of solid iron. *Geophysical Research Letters*, *44*, 128–134.
Di Tolla, F. D., & Ronchetti, M. (1993). Applicability of Nosé isothermal reversible dynamics. *Physical Review E*, *48*(3), 1726–1726.
Dubrovinsky, L. S., Saxena, S. K., Dubrovinskaia, N. A., Rekhi, S., & Le Bihan, T. (2000). Gruneisen parameter of ε-iron up to 300 GPa from in-situ X-ray study. *American Mineralogist*, *85*(2), 386–386.
Fei, Y., & Brosh, E. (2014). Experimental study and thermodynamic calculations of phase relations in the Fe-C system at high pressure. *Earth and Planetary Science Letters*, *408*, 155–162.
Huang, H., Fei, Y., Cai, L., Jing, F., Hu, X., Xie, H., et al. (2011). Evidence for an oxygen-depleted liquid outer core of the Earth. *Nature*, *479*(7374), 513–516.
Huang, L., Skorodumova, N. V., Belonoshko, A. B., Johansson, B., & Ahuja, R. (2005). Carbon in iron phases under high pressure. *Geophysical Research Letters*, *32*(21), 1–4.
Ichikawa, H., & Tsuchiya, T. (2015). Atomic transport property of Fe–O liquid alloys in the Earth's outer core P, T condition. *Physics of the Earth and Planetary Interiors*, *247*, 27–35.
Koper, K. D., & Pyle, M. L. (2004). Observations of PKiKP/PcP amplitude ratios and implications for Earth structure at the boundaries of the liquid core. *Journal of Geophysical Research*, *109*, B03301–B03301.
Kresse, G., & Furthmüller, J. (1996). Efficiency of ab-initio total energy calculations for metals and semiconductors using a plane-wave basis set. *Comput. Mater. Sci.*, *6*(1), 15–50.
Kresse, G., & Hafner, J. (1993). *Ab initio* molecular dynamics for open-shell transition metals. *Physical Review B*, *48*(17), 13,115–13,115.
Kresse, G., & Joubert, D. (1999). From ultrasoft pseudopotentials to the projector augmented-wave method. *Physical Review B*, *59*(3), 1758–1758.
Li, Y., Korzhavyi, P. A., Sandström, R., & Lilja, C. (2017). Impurity effects on the grain boundary cohesion in copper. *Physical Review Materials*, *1*(7), 070602. (R)
Li, Y., Vočadlo, L., Alfè, D., & Brodholt, J. (2017). Mg partitioning between solid and liquid iron under extreme conditions. *Physics of the Earth and Planetary Interiors*, *274*, 218–221.
Li, Y., Vočadlo, L., & Brodholt, J. (2018). The elastic properties of *hcp*-Fe alloys under the conditions of the Earth's inner core. *Earth and Planetary Science Letters*, *493*, 118–127.
Li, Y., Vočadlo, L., Brodholt, J., & Wood, I. G. (2016). Thermoelasticity of Fe_7C_3 under inner core conditions. *Journal of Geophysical Research: Solid Earth*, *121*, 5828–5837.
Lord, O. T., Walter, M. J., Dasgupta, R., Walker, D., & Clark, S. M. (2009). Melting in the Fe–C system to 70 GPa. *Earth and Planetary Science Letters*, *284*(1), 157–167.
Mao, Z., Lin, J.-F., Liu, J., Alatas, A., Gao, L., Zhao, J., & Mao, H.-K. (2012). Sound velocities of Fe and Fe-Si alloy in the Earth's core. *Proceedings of the National Academy of Sciences*, *109*(26), 10,239–10,244.
Martorell, B., Vočadlo, L., Brodholt, J., & Wood, I. G. (2013). Strong premelting effect in the elastic properties of *hcp*-Fe under inner-core conditions. *Science*, *342*(6157), 466–468.
Mashino, I., Miozzi, F., Hirose, K., Morard, G., & Sinmyo, R. (2019). Melting experiments on the Fe–C binary system up to 255 GPa: Constraints on the carbon content in the Earth's core. *Earth and Planetary Science Letters*, *515*, 135–144.
McDonough, W. F., & Sun, S. S. (1995). The composition of the Earth. *Chemical Geology*, *120*(3), 223–253.
Nosé, S. (1984). A unified formulation of the constant temperature molecular dynamics methods. *Journal of Chemical Physics*, *81*(1), 511–519.
Perdew, J. P., & Wang, Y. (1992). Accurate and simple analytic representation of the electron-gas correlation energy. *Physical Review B*, *45*, 13,244–13,249.
Posner, E. S., Steinle-Neumann, G., Vlček, V., & Rubie, D. C. (2017). Structural changes and anomalous self-diffusion of oxygen in liquid iron at high pressure. *Geophysical Research Letters*, *44*(8), 3526–3534.
Pozzo, M., Davies, C., Gubbins, D., & Alfè, D. (2019). The FeO content of Earth's Liquid Core. *Physical Review X*, *9*, 041018.
Stevenson, D. J. (1981). Models of the Earth's Core. *Science*, *214*(4521), 611–611.
Tkalčić, H., Kennett, B. L. N. N., & Cormier, V. F. (2009). On the inner–outer core density contrast from PKiKP/PcP amplitude ratios and uncertainties caused by seismic noise. *Geophysical Journal International*, *179*(1), 425–443.
Togo, A., & Tanaka, I. (2015). First principles phonon calculations in materials science. *Scripta Materialia*, *108*, 1–5.
Tsuno, K., Grewal, D. S., & Dasgupta, R. (2018). Core-mantle fractionation of carbon in Earth and Mars: The effects of sulfur. *Geochimica et Cosmochimica Acta*, *238*, 477–495.
Vočadlo, L., Alfè, D., Gillan, M. J., & Price, G. D. (2003). The properties of iron under core conditions from first principles calculations. *Physics of the Earth and Planetary Interiors*, *140*(1), 101–125.
Wood, B. J., Li, J., & Shahar, A. (2013). Carbon in the core: Its influence on the properties of core and mantle. *Reviews in Mineralogy & Geochemistry*, *75*, 231–250.
Zhang, Y., & Yin, Q.-Z. (2012). Carbon and other light element contents in the Earth's core based on first-principles molecular dynamics. *Proceedings of the National Academy of Sciences*, *109*(48), 19,579–19,583.